



Highly active and humidity resistive perovskite LaFeO₃ based catalysts for efficient ozone decomposition

Shuyan Gong^{a,b}, Zheng Xie^a, Weiman Li^{a,b}, Xiaofeng Wu^a, Ning Han^{a,c,*}, Yunfa Chen^{a,c,*}

^a State Key Laboratory of Multiphase Complex Systems, Institute of Process Engineering, Chinese Academy of Sciences, Beijing, 100190, PR China

^b University of Chinese Academy of Sciences, No. 19A Yuquan Road, Beijing, 100049, PR China

^c Center for Excellence in Regional Atmospheric Environment, Institute of Urban Environment, Chinese Academy of Sciences, Xiamen, 361021, PR China

ARTICLE INFO

Keywords:

Ozone decomposition
Perovskite LaFeO₃
Humidity resistance
In-situ Raman spectroscopy
Stability

ABSTRACT

Nowadays, it is still challenging to prepare highly active O₃ decomposition catalyst, especially with high water resistance used in harsh environments such as high relative humidity (RH). Herein, perovskite LaFeO₃ based catalysts are synthesized by a facile sol-gel method, which show far higher O₃ decomposition activity of 70–80% than the commonly used Fe₂O₃ counterpart of 0% at RH 90% and room temperature. Furthermore, 5% mol Ni is effectively doped into LaFeO₃ substituting part of Fe as verified by X-ray diffraction and X-ray photoelectron spectroscopy, which enhances the RH resistance with a stable > 90% conversion efficiency on 1000 ppm O₃ at RH 90% and room temperature in a test period of 4.0 h. The temperature programmed desorption results show that the H₂O desorption temperature decreases from 180 to 480 °C of Fe₂O₃ to < 100 °C for LaFeO₃ and LaFe_{0.95}Ni_{0.05}O₃, which contributes to the easy desorption of H₂O and thus high RH resistance of these perovskite materials. Importantly, the in-situ Raman spectra show deformation of Fe₂O₃ in O₃ decomposition reaction at high RH, leading to accumulation of intermediate O₂²⁻ and thus depression of catalytic activity. However, the perovskite materials show neither deformation nor O₂²⁻ accumulation, corresponding well with the high activity at high RH. All these results show the potential of these highly active and RH resistive perovskite catalysts for decomposition of ozone under harsh environments.

1. Introduction

Ozone is well known as a beneficial constituent of the stratosphere which shields living organisms from harmful ultraviolet radiations. However, at the ground level, it is harmful to the living creatures and also associated with the formation of photochemical smog [1–4]. Besides, due to its strong oxidative property, ozone is widely used in large volumes in several large-scale industries such as water purification [5], foods sterilization [6] and pulp processing [7], where the off gas from the oxidation process still contains a large amount of residual ozone that is often far beyond the admissible levels. In the meanwhile, ozone can also be generated in the indoor environment by photocopiers, laser printers and fax machines, which can cause health problems to human beings including neurological diseases, respiratory illness and reduced immune system function [8,9]. Consequently, ozone has long been recognized as one of the criteria air pollutants, and the removal of residual ozone from air is technologically important due to its relatively

long half-life of 160 h in atmosphere at 25 °C [10].

Catalytic decomposition is one of the most effective and economic methods to eliminate ozone. Noble metal catalysts such as Pt [11], Au [12] and Ag [13] nanoparticles are previously selected for effective degradation of ozone, which are however limited by the high cost. In recent years, transition metal oxides are more preferred due to the low-cost and relatively high efficiency [14–16]. Among them, MnO_x [17,18] and FeO_x [19,20] based oxides are the most widely and effectively used catalysts. However, the catalytic activity of these transition metal oxides is usually negatively affected by water vapor, which limits their practical application. For example, Zhang et al. observed that ozone removal efficiency of α-MnO₂ catalyst decreased from 97% to about 35%, when the RH increased from < 5% to 90% [21]. Thus it is highly desired to develop highly efficient and stabilized ozone catalytic materials, especially with high humidity resistive property working in harsh environments.

Perovskite-type mixed oxides with an ABO₃ general formula (with a

* Corresponding author at: P.O. Box 353, Beijing, 100190, PR China.

** Corresponding author at: State Key Laboratory of Multiphase Complex Systems, Institute of Process Engineering, Chinese Academy of Sciences, Beijing, 100190, PR China.

E-mail addresses: nhan@ipe.ac.cn (N. Han), chenyf@ipe.ac.cn (Y. Chen).

<https://doi.org/10.1016/j.apcatb.2018.09.041>

Received 22 April 2018; Received in revised form 11 September 2018; Accepted 15 September 2018

Available online 16 September 2018

0926-3373/ © 2018 Published by Elsevier B.V.

lanthanide in the A-position and a transition metal in the B-position) have demonstrated high potential in environmental heterogeneous catalysis due to their high stability and durability, low price, and tunable compositions [22–27]. In specific, LaFe-based perovskite seems to present improved stability in catalytic reaction compared with Mn- and Co-based structures [28]. In this study, a series of LaFe-based perovskites including pristine and nonstoichiometric LaFeO₃ as well as transition metal ions (Mn, Ni) doped LaFeO₃ are synthesized by citric sol-gel method and evaluated for ozone decomposition. The results indicate that LaFeO₃ exhibited far higher ozone catalytic performance at RH 90% than the commonly used Fe₂O₃ counterpart, and the Ni dopant (LaFe_{0.95}Ni_{0.05}O₃) further enhanced the humidity resistance, with > 90% efficiency in harsh environment of 1000 ppm O₃, RH 90% and space velocity of 240,000 mL g⁻¹ h⁻¹ at room temperature. The mechanism is proposed as the stabilized [FeO₆] structure in LaFeO₃ as compared with that in Fe₂O₃, which is investigated in detail by H₂O temperature programmed desorption, and the in-situ Raman spectroscopy during the O₃ catalytic reaction.

2. Experimental

2.1. Preparation of samples

Pristine LaFeO₃ was synthesized by citric sol-gel method referring to previous literature [29]. Analytical grade La(NO₃)₃·6H₂O, Fe(NO₃)₃·9H₂O, Ni(NO₃)₂·6H₂O, Mn(NO₃)₂ solution (50 wt. %) and citric acid were used as raw materials. Typically, stoichiometric amount of La(NO₃)₃·6H₂O and Fe(NO₃)₃·9H₂O were dissolved in deionized water under magnetic stirring to obtain a homogeneous solution. Then, citric acid was added to the solution as a chelator with the same equivalents to the sum molar amount of metal nitrates. Ammonia was slowly dropped into the mixture to maintain the pH value at 6–7. Afterwards, the solution was kept stirred continuously at 75 °C until a stabilized sol was formed. The sol was dried at 130 °C overnight, which then turned into a puffy and porous dry gel. The gel was further combusted automatically by ignition and then annealed at 600 °C for 2 h. Pure Fe₂O₃ and La₂O₃ were obtained using the same method by merely adding the precursors of Fe or La nitrates, and the other experimental conditions were kept the same as those of LaFeO₃. Nonstoichiometric La_{1.5}FeO₃, LaFe_{1.5}O₃ and transition metal ion (Mn, Ni) doped LaFe_{0.95}Mn_{0.05}O₃ and LaFe_{0.95}Ni_{0.05}O₃ were also synthesized by the same method.

2.2. Characterizations

The morphology and element distribution of samples were characterized by scanning electron microscope (SEM, JEOL JSM-6700 F, Japan, 15 kV, 10 mA), equipped with an energy dispersive X-ray detector (EDS). The microstructures of samples were observed on a transmission electron microscope (TEM, JEOL JEM-2100 F, 200 kV). The crystal structure was characterized by powder X-ray diffraction (XRD) on a Panalytical X'Pert PRO system (40 kV, 40 mA), with Cu-Kα radiation. The surface chemical states were determined by X-ray photoelectron spectroscopy (XPS) on an XLESCALAB 250Xi electron spectrometer from VG Scientific with monochromatic Al-Kα radiation. The binding energy was calibrated to the C1 s line at 284.8 eV. N₂ adsorption-desorption isotherm were measured at 77 K on an automatic surface analyzer (SSA-7300, China), and the BET specific surface areas and pore size distributions were obtained according to the Brunauer-Emmett-Teller (BET) and Barrett-Joyner-Halenda (BJH) methods. Fourier transform infrared spectroscopy (FTIR) was performed on Hitachi FTIR-8900 between 4000 and 400 cm⁻¹.

NH₃-, H₂O- and O₂-temperature programmed desorption (TPD) and H₂-temperature programmed reduction (TPR) experiments were carried out on Automated Catalyst Characterization System (Autochem 2920). In NH₃-TPD, 0.10 g catalysts were degassed under He flow at 350 °C, and then the samples were subjected to a mixture of 10% NH₃ in He at a

flow rate of 30 mL min⁻¹ at 50 °C. The excess NH₃ was removed by passing He through the catalysts. The temperature was then ramped to 900 °C at a rate of 10 °C min⁻¹ under He flow and desorption data was taken. In H₂O-TPD, 50 mg sample was placed in a reaction tube and the surface H₂O was removed by heating at 600 °C for 1 h and purging with He gas. After that, the sample was saturated with H₂O in 30 times pulse H₂O (50 mL min⁻¹) flow at 50 °C. Then, desorption of H₂O was carried out from 50 °C to 600 °C at a heating rate of 10 °C min⁻¹ purged with He. In O₂-TPD, 50 mg sample was pre-treated at 600 °C for 1 h under He flow (30 mL min⁻¹), and exposed to 5% O₂-He for 2 h. After that, the sample was cooled to room temperature and then purged by He for 1 h to stabilize the mass spectrometer base line. Finally, the reactor was heated at a heating rate of 10 °C min⁻¹ from room temperature to 900 °C, and the desorbed oxygen signal was collected by the mass spectrometer detector. In H₂-TPR, about 50 mg powder (40–60 mesh) was loaded in a U-shaped quartz reactor (10% H₂ balanced with Ar, 25 mL min⁻¹) and the temperature was raised to 750 °C with a rate of 10 °C min⁻¹.

The in-situ Raman spectra were recorded on Jobin-Yvon LABRAM HR800 Raman Microscope with a resolution of 2 cm⁻¹, at excitation of 532 nm. The catalyst of ~100 mg was put into an in-situ reaction cell and Raman spectra were acquired under air/oxygen flow and under air/ozone flow in dry and humid conditions with 1000 ppm ozone.

2.3. Catalytic activity evaluation

The ozone degradation performance was measured in the U-shaped quartz tube reactor (φ5.5 mm) using 50 mg (40–60 mesh) catalyst mixed with 450 mg quartz sand at room temperature. Ozone was generated at 200 or 1000 ppm by a commercial ozone generator (COM-AD-01-OEM, ANSEROS COMPANY, Anshan, China), and the total space velocity (SV) was 240,000 mL g⁻¹ h⁻¹ with a gas flow of 200 mL min⁻¹. The inlet and outlet ozone concentrations (C_{inlet} and C_{outlet}) were analyzed by an ozone monitor (model 106 M, 2B Technologies, USA) and ozone conversion was calculated as 100% × (C_{inlet} - C_{outlet})/C_{inlet}. Water vapor was produced by bubbling the water with the air flow, and the relative humidity (RH) was measured by a humidity and temperature sensor (center 310 RS-232, TES, Taiwan).

3. Results and discussion

3.1. Crystal structural and textural properties of La₂O₃, Fe₂O₃ and LaFeO₃

Fig. 1 shows XRD patterns of lanthanum oxide, iron oxide and lanthanum ferrite, which show the hexagonal phase La₂O₃ (PDF# 01-074-2430), rhombohedral phase α-Fe₂O₃ (Hematite, PDF# 01-089-8104), and orthorhombic perovskite phase LaFeO₃ (PDF# 00-037-1493).

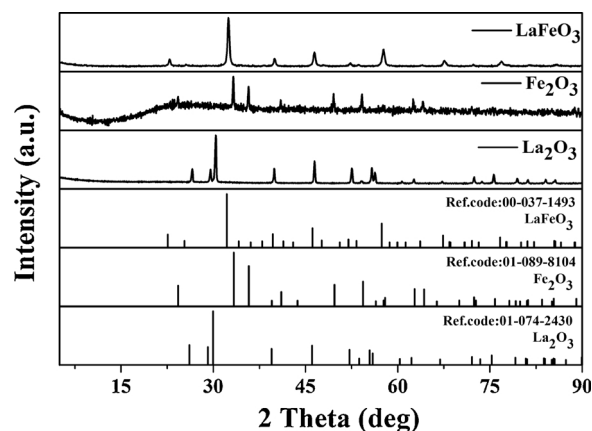


Fig. 1. Powder XRD patterns of La₂O₃, Fe₂O₃ and LaFeO₃ materials and corresponding standard card.

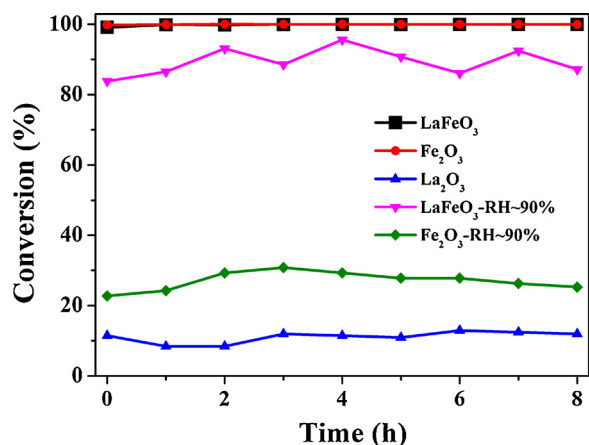


Fig. 2. Ozone conversion as a function of reaction time over La_2O_3 , Fe_2O_3 and LaFeO_3 . (Ozone inlet concentration: 200 ppm, $T = 25^\circ\text{C}$, $\text{SV} = 240,000 \text{ mL g}^{-1} \text{ h}^{-1}$, dry air or air with RH ~ 90% carrier gas).

1493). It is noted that all the LaFeO_3 peaks are designated to the perovskite phase with no miscellaneous peaks of La or Fe oxides, showing the phase purity of this material. This is also in good agreement with the EDS analysis of LaFeO_3 in Table S1 where the atomic ratio of La:Fe:O is 1:1:3, indicating the successful synthesis of stoichiometric LaFeO_3 . Fig. S1 shows the SEM photographs and N_2 adsorption-desorption isotherm of prepared Fe_2O_3 , La_2O_3 and LaFeO_3 . Fe_2O_3 exhibits dense surface structure and its corresponding surface area is $6.5 \text{ m}^2 \text{ g}^{-1}$ as shown in Fig. S1a and b. In contrast, La_2O_3 and LaFeO_3 display relatively loose structure and higher surface area of $19.5 \text{ m}^2 \text{ g}^{-1}$ and $18.7 \text{ m}^2 \text{ g}^{-1}$, respectively (Fig. S1c–f).

3.2. Catalytic activity test of La_2O_3 , Fe_2O_3 and LaFeO_3

The ozone degradation efficiencies of La_2O_3 , Fe_2O_3 and LaFeO_3 were then assessed at room temperature with ozone concentration of 200 ppm as shown in Fig. 2. It is shown that ozone conversion efficiencies of Fe_2O_3 and LaFeO_3 are similar and keep at 100% during 8 h of continuous operation at dry condition, while La_2O_3 exhibits a low ozone conversion efficiency of about 10%. In order to explore the RH resistive property of Fe_2O_3 and LaFeO_3 , a high RH level of 90% was introduced into ozone decomposition reactor. It is noted that the activity of Fe_2O_3 rapidly decreases and ozone conversion is only about 25% after 8 h test. However, though RH also has some negative effects on catalyst LaFeO_3 , the efficiency keeps as high as above 85% after 8 h of continuous operation at RH 90% as shown in Fig. 2. Therefore, LaFeO_3 exhibits higher moisture resistance compared with pure Fe_2O_3 .

3.3. Crystal structural and textural properties of LaFeO_3 and modified LaFeO_3

Generally, the functional properties of perovskite materials can be adjusted either by modulating the crystalline structure and composition or by incorporating different metal ions into the perovskite lattice [30–33]. In this study, we altered the molar ratio of La/Fe and substituted Fe by some transition metal ions (Mn, Ni), and further explored their abilities for ozone decomposition. The phase purity and crystallinity of as-prepared nonstoichiometric $\text{LaFe}_{1.5}\text{O}_3$, $\text{La}_{1.5}\text{FeO}_3$ and doped LaFeO_3 were examined by XRD measurement and the results were shown in Fig. 3a. The main diffraction peaks of $\text{LaFe}_{1.5}\text{O}_3$ and $\text{La}_{1.5}\text{FeO}_3$ are attributed to the perovskite structure of LaFeO_3 . And additional peaks ascribed to Fe_2O_3 (the red framed area) and La_2O_3 (the green framed area) are detected in $\text{LaFe}_{1.5}\text{O}_3$ and $\text{La}_{1.5}\text{FeO}_3$, respectively, suggesting that excessive Fe and La are in the form of metal oxides. The diffraction peaks of doped samples are consistent with perovskite

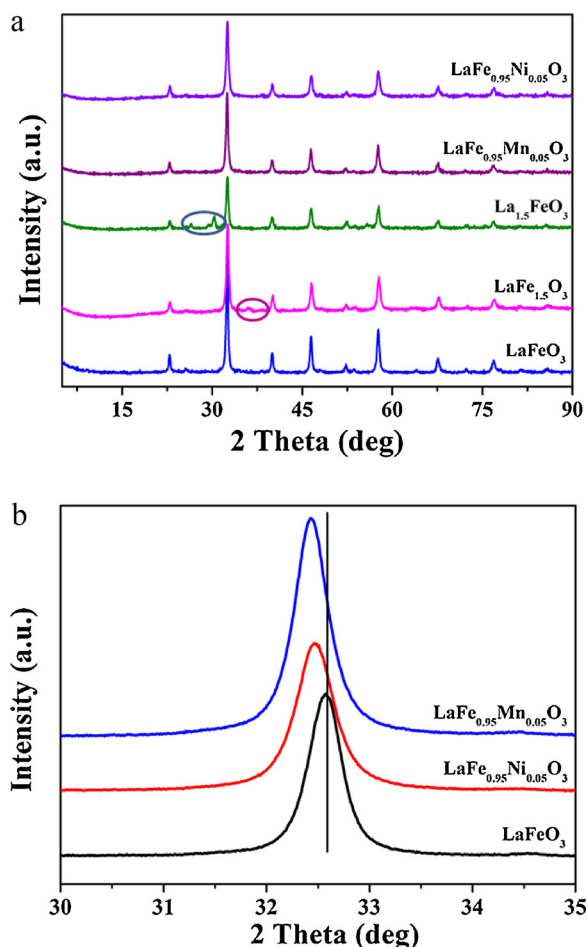


Fig. 3. (a) XRD patterns of LaFeO_3 , $\text{LaFe}_{1.5}\text{O}_3$, $\text{La}_{1.5}\text{FeO}_3$, $\text{LaFe}_{0.95}\text{Ni}_{0.05}\text{O}_3$ and $\text{LaFe}_{0.95}\text{Mn}_{0.05}\text{O}_3$ and (b) The high resolution XRD patterns of LaFeO_3 , $\text{LaFe}_{0.95}\text{Ni}_{0.05}\text{O}_3$ and $\text{LaFe}_{0.95}\text{Mn}_{0.05}\text{O}_3$.

structured phase (PDF# 00-037-1493), and no other peaks due to doped metal oxide phases are observed. Meanwhile the main peak corresponding to plane (121) of $\text{LaFe}_{0.95}\text{Mn}_{0.05}\text{O}_3$ and $\text{LaFe}_{0.95}\text{Ni}_{0.05}\text{O}_3$ shifts to lower 2θ values compared with that of LaFeO_3 as shown by the high resolution XRD (Fig. 3b). The reason for this shift is that the radii of dopants Mn^{3+} (0.066 nm) and Ni^{2+} (0.069 nm) are larger than that of Fe^{3+} (0.064 nm), so the crystal expands after partial replacement of Fe by Mn and Ni ions, leading to the increase of interplanar spacing [34]. This phenomenon indicates that the dopants are well incorporated into the perovskite structure [35]. Fig. S2 presents the SEM images of prepared samples, where the morphologies of nonstoichiometric $\text{LaFe}_{1.5}\text{O}_3$, $\text{La}_{1.5}\text{FeO}_3$ and doped LaFeO_3 are similar to that of pristine LaFeO_3 . High resolution SEM image (Fig. S2a) shows that LaFeO_3 is composed of clustered nanoparticles, and the grain sizes (as listed in Table S2) of these samples are determined by applying the Scherrer equation. The crystal domain sizes are around 20 nm and the corresponding specific surface areas range from $13.6 \text{ m}^2 \text{ g}^{-1}$ (for $\text{La}_{1.5}\text{FeO}_3$) to $23.4 \text{ m}^2 \text{ g}^{-1}$ (for $\text{LaFe}_{1.5}\text{O}_3$). Table S2 also displays the atomic ratio of Fe/La and doped M/La in EDS results. On one hand, nonstoichiometric $\text{LaFe}_{1.5}\text{O}_3$ and $\text{La}_{1.5}\text{FeO}_3$ samples have a typical value of Fe/La and La/Fe around 1.5. On the other hand, the M/La molar ratios of doped samples are almost 5%, which is consistent with the corresponding experimental ratio. The result demonstrates that the samples are synthesized in good agreement with experimental plan.

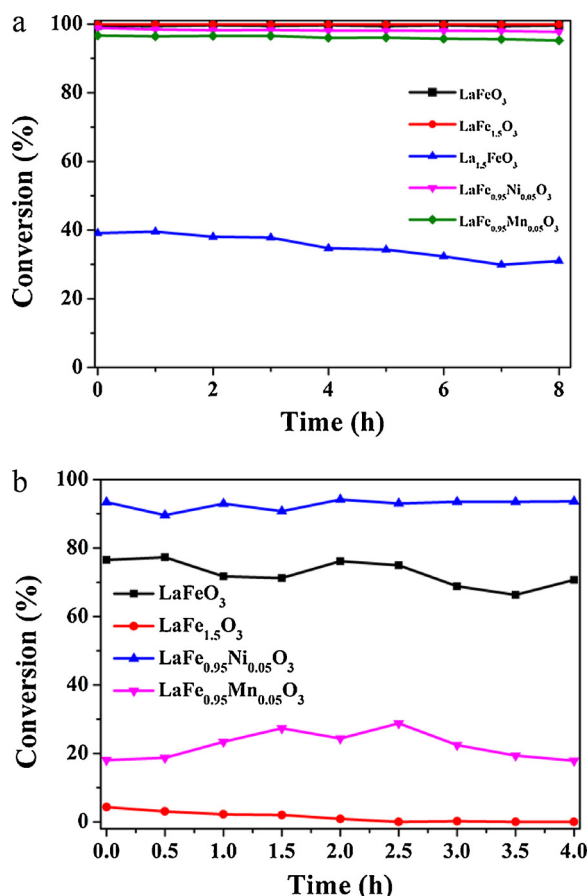


Fig. 4. Ozone conversion as a function of reaction time over prepared LaFe-based perovskite samples at ozone inlet concentration: 1000 ppm, $T = 25^\circ\text{C}$, $\text{SV} = 240,000\text{ mL g}^{-1}\text{ h}^{-1}$, (a) in dry air and (b) RH $\sim 90\%$.

3.4. Catalytic activity test of LaFeO_3 and modified LaFeO_3

To further explore the activity of the modulated catalysts at harsh conditions, ozone decomposition was performed at high ozone concentration of 1000 ppm as shown in Fig. 4. The La-rich $\text{La}_{1.5}\text{FeO}_3$ is the least active among these catalysts, with an ozone conversion of only 30.9% after 8 h test in dry air as shown in Fig. 4a. Obviously it is due to the formation of La_2O_3 (confirmed by XRD in Fig. 3a), which exhibits poor activity for ozone decomposition as shown in Fig. 2. On the other side, LaFeO_3 and $\text{LaFe}_{1.5}\text{O}_3$ have higher catalytic activities of nearly 100% after 8 h test, and doped LaFeO_3 catalysts also exhibit good catalytic performance of over 95% after an 8 h test: $\text{LaFe}_{0.95}\text{Ni}_{0.05}\text{O}_3$ (97.7%) and $\text{LaFe}_{0.95}\text{Mn}_{0.05}\text{O}_3$ (95.2%). To test the humidity resistance, the catalytic activities were measured at high RH $\sim 90\%$ as shown in Fig. 4b. It is noted that ozone conversion of $\text{LaFe}_{1.5}\text{O}_3$ dramatically drops from nearly 100% in dry air (Fig. 4a) to 0% after 4 h test under high RH, so does Fe_2O_3 as shown in Fig. S3. This result could be attributed to the formed Fe_2O_3 by excessive Fe, which has been proven to have very low resistance to water vapor (shown in Figs. 2 and S3). On the other side, ozone decomposition efficiency of LaFeO_3 only decreases a little from nearly 100% in dry air to $> 70\%$ after 4 h continuous operation at RH 90%. Furthermore, $\text{LaFe}_{0.95}\text{Ni}_{0.05}\text{O}_3$ exhibits better ozone decomposition performance (93%) under high RH compared with pure LaFeO_3 , showing the effect of dopant on the stability of the perovskite. We make a comparison with some recent reported literatures [15,18,21,36–40] shown in Table S3, it suggests that the ozone removal performance LaFeO_3 and $\text{LaFe}_{0.95}\text{Ni}_{0.05}\text{O}_3$ in our study are ones of the highest compared with listed catalysts, especially in the flow of high RH. However, the dopant should be well chosen as Mn doped

LaFeO_3 ($\text{LaFe}_{0.95}\text{Mn}_{0.05}\text{O}_3$) presents much lower activity with 17.5% ozone removal efficiency at RH 90%, which would be addressed in the following sections.

In addition, specific catalytic activity (SA) is used for comparison of intrinsic catalytic activities of different catalysts in this study., as expressed as the number of moles of decomposed ozone per square meter per hour, i.e. $\text{SA} (\text{mol m}^{-2}\text{ h}^{-1}) = \text{CXF}/(22.4\text{WS})$, where C is the feed concentration (ppm) of ozone, X is the conversion of ozone, F is the total volumetric flow rate (L h^{-1}), W is the weight of catalyst (g), and S is the surface area of the catalyst ($\text{m}^2\text{ g}^{-1}$). As seen from Table S4, SA of Fe_2O_3 in dry air is the highest due to its lowest surface area, though the ozone conversion (95%) is not as high as that of LaFeO_3 (100%). SA of other perovskite LaFeO_3 based catalysts are similar (around $5 \times 10^{-4}\text{ mol m}^{-2}\text{ h}^{-1}$) in dry air except $\text{La}_{1.5}\text{FeO}_3$. It is noticed that SA of Fe_2O_3 and $\text{LaFe}_{1.5}\text{O}_3$ dramatically decrease with several orders of magnitude under high RH condition because of the invalid Fe_2O_3 component with little water resistance. As for $\text{LaFe}_{0.95}\text{Ni}_{0.05}\text{O}_3$ and LaFeO_3 , SA obtained at high RH is a bit lower than that acquired in dry air and $\text{LaFe}_{0.95}\text{Ni}_{0.05}\text{O}_3$ exhibits the best intrinsic activity in presence of water in terms of SA. A more obvious decrease in SA of $\text{LaFe}_{0.95}\text{Mn}_{0.05}\text{O}_3$ is observed compared with $\text{LaFe}_{0.95}\text{Ni}_{0.05}\text{O}_3$ and LaFeO_3 when water vapor is added to the reaction gas. By comparing SA of catalysts, it can be seen that though Fe_2O_3 exhibits a bit higher intrinsic catalytic abilities to ozone decomposition in dry air it has little humidity resistance and even becomes invalid at high RH. In contrast, $\text{LaFe}_{0.95}\text{Ni}_{0.05}\text{O}_3$ and LaFeO_3 not only present comparable ozone removal performance to that of Fe_2O_3 in dry air but also show desirable catalytic activity in a gas flow with water.

3.5. TEM and surface atom state analyses of samples

In order to further identify the morphology of highly efficient LaFeO_3 and $\text{LaFe}_{0.95}\text{Ni}_{0.05}\text{O}_3$, TEM was used to characterize the obtained samples as shown in Fig. 5. It is seen from Fig. 5a and b that LaFeO_3 and $\text{LaFe}_{0.95}\text{Ni}_{0.05}\text{O}_3$ are consisted of numerous irregular nanoparticles. The lattice images of the nanoparticles are shown in Fig. 5c and d with a characteristic lattice spacing of 0.39 nm, which is in agreement with the (101) plane of perovskite LaFeO_3 . The selected area diffraction patterns (SAED) in Fig. 5e and f show the polycrystalline crystallography of LaFeO_3 and $\text{LaFe}_{0.95}\text{Ni}_{0.05}\text{O}_3$, and the discontinuous rings correspond well to {121}, {220}, {240}, {242} and {101}, {121}, {202}, {240} planes of LaFeO_3 and $\text{LaFe}_{0.95}\text{Ni}_{0.05}\text{O}_3$.

In order to explore the surface element states, XPS spectra of prepared samples are reported in Fig. 6. The Fe 2p spectra (Fig. 6a) show that there is a shift toward lower binding energies from Fe_2O_3 to LaFeO_3 and $\text{LaFe}_{0.95}\text{Ni}_{0.05}\text{O}_3$. The negative core level shift indicates the increase of the electron density in Fe 2p of LaFeO_3 and $\text{LaFe}_{0.95}\text{Ni}_{0.05}\text{O}_3$ compared with that of Fe_2O_3 . The Fe 2p spectra are then deconvoluted into two peaks with binding energies at 710 eV and 711 eV ascribed to Fe^{2+} and Fe^{3+} [31,41] in Fig. 6b. A quantitative analysis of surface Fe^{2+} and Fe^{3+} is summarized in Table 1, where it is seen that the molar ratio of Fe^{2+} is higher for LaFeO_3 (45.2%) and $\text{LaFe}_{0.95}\text{Ni}_{0.05}\text{O}_3$ (45.8%) than that of Fe_2O_3 (31.0%). The shakeup satellite at around 719 eV is recognized as characteristic peak of Fe^{3+} ions [42,43]. Then the intensity of shakeup satellite in LaFeO_3 and $\text{LaFe}_{0.95}\text{Ni}_{0.05}\text{O}_3$ are obviously lower than that in Fe_2O_3 spectrum as seen in Fig. 6a and b, which also suggests that there are more abundant Fe^{2+} ions on the surface of LaFeO_3 and $\text{LaFe}_{0.95}\text{Ni}_{0.05}\text{O}_3$ compared with Fe_2O_3 . The relatively higher Fe^{2+} ratio would be attributed to the pH adjustment by ammonia in the preparation process, as the control sample prepared without ammonia addition possesses a relatively lower ratio as shown in supporting information Figs. S4 and Table S5. This high Fe^{2+} content on the surface might be attributed to the surface reduction by residual ammonia in the annealing which (62.14% Fe^{2+}) was also observed in the literature [44]. In the meanwhile, the O 1s spectra are also present in Fig. 6c, and two kinds of surface oxygen species can be distinguished

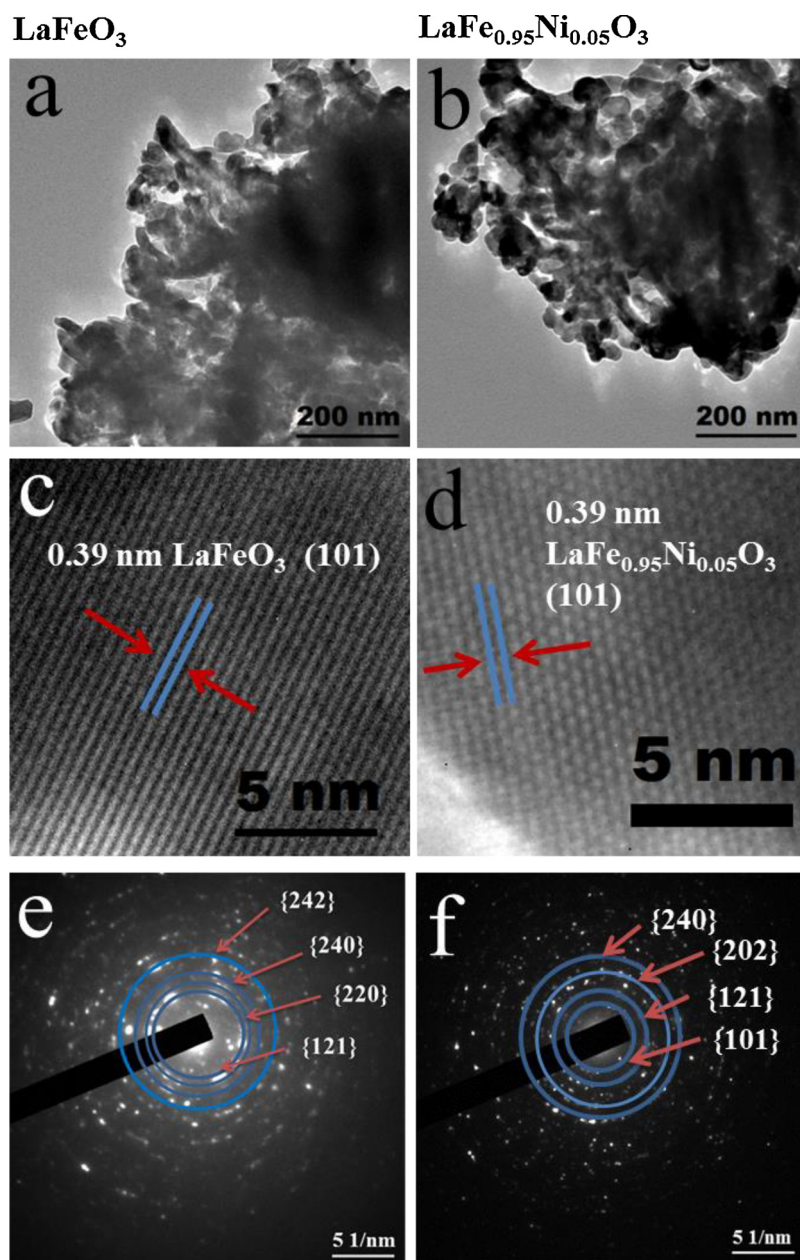


Fig. 5. (a–b) TEM images of LaFeO_3 and $\text{LaFe}_{0.95}\text{Ni}_{0.05}\text{O}_3$, (c–d) HRTEM images of LaFeO_3 and $\text{LaFe}_{0.95}\text{Ni}_{0.05}\text{O}_3$ and (e–f) SAED of LaFeO_3 and $\text{LaFe}_{0.95}\text{Ni}_{0.05}\text{O}_3$.

as shown in Fig. 6d. Lower binding energy at around 529 eV can be ascribed to the lattice oxygen species and the higher binding energy at about 531 eV can be assigned to the surface adsorbed oxygen [45]. Obviously the lattice oxygen of perovskite LaFeO_3 and doped LaFeO_3 exhibit lower binding energy than that of Fe_2O_3 , which is in accordance with the shift of Fe 2p. Moreover, LaFeO_3 and doped LaFeO_3 possess more adsorbed oxygen on their surface compared with Fe_2O_3 as marked by dotted line in Fig. 6c around 531 eV, which is consistent with previous literatures [46]. Calculated $\text{O}_{\text{ads}}/\text{O}_{\text{total}}$ atomic ratios of each oxygen species are present in Table 1, which is higher for LaFeO_3 (0.46) and $\text{LaFe}_{0.95}\text{Ni}_{0.05}\text{O}_3$ (0.51) than that of Fe_2O_3 (0.35). This is also in good consistence with the FT-IR spectra in Fig. S5 of Fe_2O_3 , LaFeO_3 and $\text{LaFe}_{0.95}\text{Ni}_{0.05}\text{O}_3$, where the band at 1629 cm^{-1} is characteristic of surface-adsorbed oxygen species [47]. According to the literature, oxygen molecules usually are adsorbed at the oxygen vacancies of catalyst surface, and oxygen vacancies are generated to maintain electrostatic balance when low metal valence state appears [36,48]. Reasonably, the trend of $\text{O}_{\text{ads}}/\text{O}_{\text{total}}$ ratios is consistent with that of

surface Fe^{2+} atomic ratios mentioned above. So by combining O_{ads} ratios with Fe^{2+} atomic ratios in our study, we can conclude the density of low valence Fe^{2+} and oxygen vacancies in LaFeO_3 and $\text{LaFe}_{0.95}\text{Ni}_{0.05}\text{O}_3$ are higher compared with other samples. It has been proved that the mixed valence in transition metal oxide is important for electron transport and could facilitate the redox process during ozone decomposition [40]. Therefore abundant $\text{Fe}^{2+}/\text{Fe}^{3+}$ redox couples existed on the surface of the LaFeO_3 and $\text{LaFe}_{0.95}\text{Ni}_{0.05}\text{O}_3$ could be responsible for their superior catalytic performances.

3.6. TPD and TPR studies

It is reported that ozone molecule exhibits basic character and could adsorb/decompose on surface acid sites of metal oxides [49,50]. Therefore, NH_3 -TPD experiments were carried out to characterize the acidity of prepared samples as shown in Fig. 7a. The specific amount of desorbed NH_3 is an indirect measurement of the global acidity, and the result is shown in Table S6. It is noticed that Fe_2O_3 shows weak NH_3

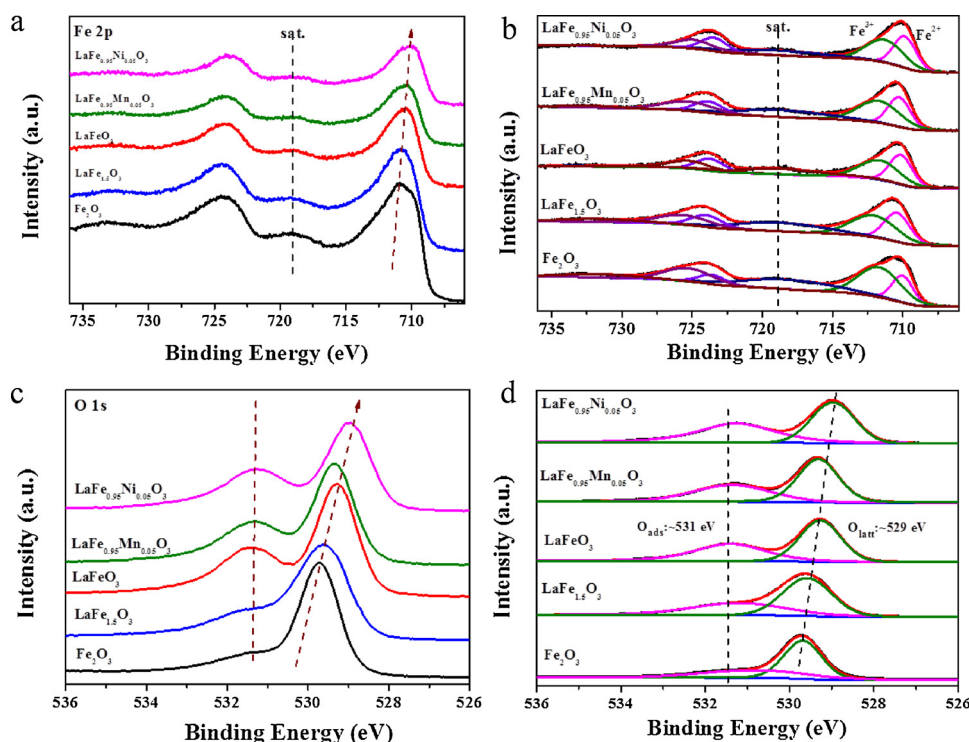


Fig. 6. XPS pattern of (a–b) Fe 2p and (c–d) O 1s for as-prepared catalysts.

desorption peaks for acidic sites, while LaFeO_3 and $\text{LaFe}_{0.95}\text{Ni}_{0.05}\text{O}_3$ display higher concentration of acidic surface sites shown in the intermediate temperature. It is reported that the low temperature desorption may originate from NH_4^+ species weakly bonded to hydroxyl surface groups and/or possible desorption of residual physical adsorbed ammonia and intermediate temperature desorption may originate from NH_3 coordinated to Lewis acid sites [31]. Therefore, the more adsorption/reaction sites for ozone molecules over LaFeO_3 and $\text{LaFe}_{0.95}\text{Ni}_{0.05}\text{O}_3$ would contribute to their higher activity and humidity resistance compared with that of Fe_2O_3 .

The mainly catalytic difference of perovskite LaFeO_3 and Fe_2O_3 is the high resistance to water vapor as shown in Figs. 2 and 4, so the H_2O -TPD is further characterized to analyze the humidity resistance: the lower of the desorption temperature, the higher resistance to water. As seen in Fig. 7b, three desorption peaks of Fe_2O_3 are observed at 180 °C, 340 °C and 480 °C. As for $\text{LaFe}_{1.5}\text{O}_3$, the first desorption peak occurs at 93 °C, and the second appears at 438 °C. Similarly, the first peak of $\text{LaFe}_{0.95}\text{Mn}_{0.05}\text{O}_3$ is at around 90 °C, and there are two extra peaks locating at 244 °C and 426 °C. However, there is only one significant desorption peak for the LaFeO_3 and $\text{LaFe}_{0.95}\text{Ni}_{0.05}\text{O}_3$ at around 90 °C, which could be attributed to desorption of dissociated water molecules. It is also reported that the hydroxyl recombinative desorption kinetics is related to the surface structure, and those reduced cation sites (Fe^{2+}) bind water weakly than the fully oxidized surface [51]. Therefore, the TPD results are in good agreement with the XPS analysis: LaFeO_3 and $\text{LaFe}_{0.95}\text{Ni}_{0.05}\text{O}_3$ with more reduced Fe^{2+} show low-temperature water

desorption. Overall, H_2O molecules are more easily to be desorbed from LaFeO_3 and $\text{LaFe}_{0.95}\text{Ni}_{0.05}\text{O}_3$, so the humidity resistance of LaFeO_3 and $\text{LaFe}_{0.95}\text{Ni}_{0.05}\text{O}_3$ is higher than those of other prepared catalysts.

H_2 -TPR profiles were performed to evaluate the reducibility of prepared samples as shown in Fig. 7c. Fe_2O_3 exhibits a reduction peak centered at 410 °C, which can be attributed the reduction of Fe_2O_3 to Fe_3O_4 . The other extensive peak at around 600 °C is ascribed to the reduction of Fe_3O_4 to FeO [52–54]. As for LaFeO_3 , La^{3+} can not be reduced under the condition of H_2 -TPR, so the observed reduction peak is ascribed to the reduction of Fe ions. There is a broad reduction peak between 300 °C and 500 °C in the case of LaFeO_3 , which can be ascribed to the multiple-step reduction of Fe^{3+} to Fe^{2+} on surface and in bulk of LaFeO_3 [28,31,55]. $\text{LaFe}_{1.5}\text{O}_3$ exhibits a weak reduction bands in the temperature range from 300 to 500 °C and a strong reduction around 600 °C. The first broad peak is ascribed to overlapping reduction bands of Fe^{3+} to Fe^{2+} in LaFeO_3 phase and the reduction of Fe_2O_3 to Fe_3O_4 in Fe_2O_3 phase formed by excessive Fe. The later peak at 600 °C is related to the reduction of Fe_3O_4 to FeO in Fe_2O_3 phase. The reduction of Ni^{2+} to Ni^0 in perovskite structure usually occurs at high temperature (above 800 °C) [26], so the reduction peak of $\text{LaFe}_{0.95}\text{Ni}_{0.05}\text{O}_3$ is attributed to the reduction of Fe ions. In addition, the reduction of Fe^{3+} to Fe^{2+} shifts to lower temperature in the $\text{LaFe}_{0.95}\text{Ni}_{0.05}\text{O}_3$, suggesting that lattice Ni^{2+} interacts with the iron ion, making it to be more easily reduced. The reduction peaks of Mn ions are generally around 300–500 °C [56], which overlap with the part of Fe^{3+} reduction peaks, exhibiting a broad peak in $\text{LaFe}_{0.95}\text{Mn}_{0.05}\text{O}_3$. It is reported that

Table 1
Surface composition and oxidation state of fresh and used catalysts.

Catalysts	Fe^{2+} (%) (Fresh)	Fe^{3+} (%) (Fresh)	$\text{O}_{\text{ads}}/\text{O}_{\text{total}}$ (Fresh)	Fe^{2+} (%) (Used)	Fe^{3+} (%) (Used)	$\text{O}_{\text{ads}}/\text{O}_{\text{total}}$ (Used)
Fe_2O_3	31.0	69.0	0.35	36.2	63.8	0.38
$\text{LaFe}_{1.5}\text{O}_3$	43.1	56.9	0.41	42.0	58.0	0.72
LaFeO_3	45.2	54.8	0.46	39.1	60.9	0.51
$\text{LaFe}_{0.95}\text{Mn}_{0.05}\text{O}_3$	41.4	58.6	0.43	39.6	60.4	0.51
$\text{LaFe}_{0.95}\text{Ni}_{0.05}\text{O}_3$	45.8	54.2	0.51	40.6	59.4	0.54

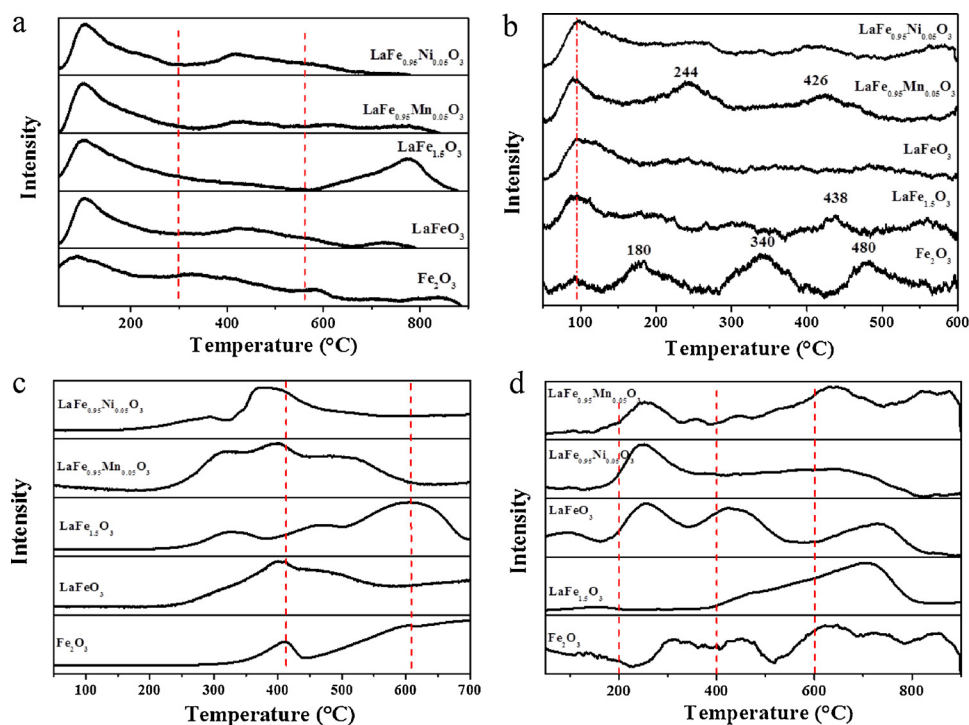


Fig. 7. (a) NH_3 -TPD, (b) H_2O -TPD, (c) H_2 -TPR and (d) O_2 -TPD profiles of prepared samples.

reducibility is correlated with the metal-oxygen (M–O) bonding of B-site cations [57] and the presence of oxygen vacancies could loosen the bond strength, making the catalyst easier to be reduced by H_2 [58]. Considering XPS analysis, LaFeO_3 has abundant oxygen vacancies and the doping of Ni further increases the amounts of oxygen vacancies. So the M–O bonds in $\text{LaFe}_{0.95}\text{Ni}_{0.05}\text{O}_3$ could be broken more easily leading to higher reducibility. While the amount of oxygen vacancies in $\text{LaFe}_{0.95}\text{Mn}_{0.05}\text{O}_3$ is even lower than that of pure LaFeO_3 due to the inappropriate doping, which may decrease the reducibility. Therefore, it can be speculated that the doping of metal cations in the catalytic system could influence the reducibility of the samples by modifying the M–O bonding of B-site cations. And the relatively more easily reduced and weaker M–O bond might favor the chemisorbed O_2^{2-} adsorption and desorption in the O_3 degradation process described in the following section.

The oxygen desorption performance was then assessed by O_2 -TPD as shown in Fig. 7d. Generally, the peak below 200°C is assigned to desorption of physically adsorbed oxygen. And the peak in the range of 200°C to 400°C is ascribed to weakly chemisorbed surface active oxygen that is adsorbed on oxygen vacancies [48]. The intermediate region (400°C – 600°C) corresponds to the desorption of near-surface oxygen and the higher temperature range above 600°C refers to the desorption of lattice oxygen [59,60]. As seen from Fig. 7d, LaFeO_3 has more surface adsorbed active oxygen (200°C – 400°C) compared with Fe_2O_3 and $\text{LaFe}_{1.5}\text{O}_3$. And the surface active oxygen desorption peak of $\text{LaFe}_{0.95}\text{Ni}_{0.05}\text{O}_3$ is even higher, which is in good agreement with the XPS analysis. The relatively higher peak intensity at lower temperature would infer the higher catalytic activity. This is also in good agreement with the literature that the existence of abundant oxygen ions on catalyst surface could facilitate the desorption of key intermediate (O_2^{2-}) during ozone decomposition [61]. In summary, LaFeO_3 and $\text{LaFe}_{0.95}\text{Ni}_{0.05}\text{O}_3$ possess large amounts of chemisorbed surface active oxygen species, which is beneficial to the catalytic performance for ozone decomposition.

3.7. Ozone decomposition mechanism

Combining with the previous literatures [62,63], the ozone decomposition reaction involves the adsorption and reaction of ozone over catalyst surface and desorption of intermediate oxygen species. The process can be expressed by following Eqs. (1–3).



During the reaction process, the release of active oxygen from the catalyst surface (Eq. 3) is the rate-determining step of ozone decomposition.

To investigate how the catalysts participate in the O_3 catalytic reaction, the surface atom state change of tested catalysts in high RH condition was investigated by XPS as shown in Table 1. It is seen that the Fe^{2+} atomic ratios of used LaFeO_3 and doped LaFeO_3 are slightly lower than that of fresh samples, indicating that some Fe^{2+} are oxidized into Fe^{3+} during ozone decomposition. However, the Fe^{2+} atomic ratios of Fe_2O_3 and $\text{LaFe}_{1.5}\text{O}_3$ remain unchanged and even a bit increase (within the error rang). Considering the low activity of Fe_2O_3 and $\text{LaFe}_{1.5}\text{O}_3$ in high RH reaction condition (as shown in Figs. 2 and 4), it can be speculated that pure Fe_2O_3 and inactive Fe_2O_3 layer over $\text{LaFe}_{1.5}\text{O}_3$ scarcely react with ozone molecular due to the accumulation of water on catalyst surface, leading to the unchanged valence of Fe. On the other side, all the used catalysts have higher $\text{O}_{\text{ads}}/\text{O}_{\text{total}}$ ratios and thus more adsorbed oxygen than fresh catalysts as shown in Table 1. This is because desorption of intermediate oxygen species is not sufficiently fast, and the catalyst surface is partly occupied by oxygen species. Therefore, the surface states correspond well to the activity of the catalysts.

In-situ Raman spectroscopy is an excellent tool to study the structure of active phase and surface intermediates at reaction conditions, which is then adopted to detect surface oxygen species and the real-time structural changes of catalysts when exposed to oxygen, ozone and ozone/water vapor reaction gases, in an aim to gain insights into the

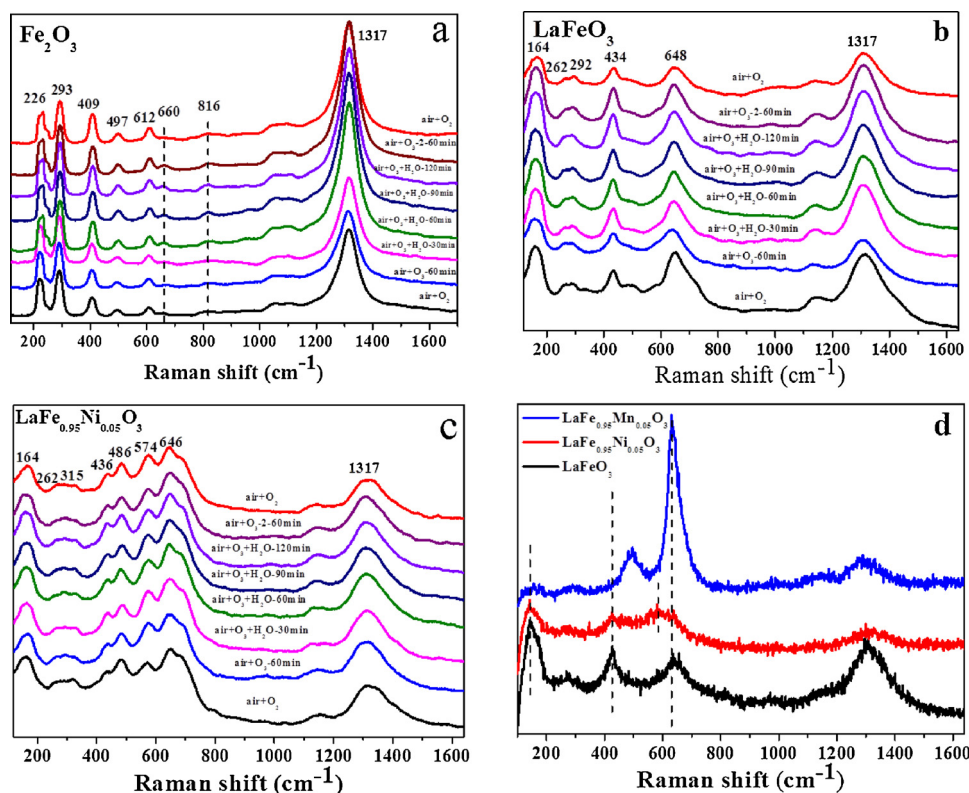


Fig. 8. (a–c) In-situ Raman spectra of Fe_2O_3 , LaFeO_3 and $\text{LaFe}_{0.95}\text{Ni}_{0.05}\text{O}_3$ under air/oxygen flow and under air/ozone flow in dry and humid conditions, (d) Raman spectra of LaFeO_3 , $\text{LaFe}_{0.95}\text{Ni}_{0.05}\text{O}_3$ and $\text{LaFe}_{0.95}\text{Mn}_{0.05}\text{O}_3$.

reaction process. Fig. 8a is the in-situ Raman spectra of Fe_2O_3 in different reaction conditions. The signals locate at 226 and 497 cm^{-1} are ascribed to two A_{1g} modes, and the bands at 293, 409, 612 cm^{-1} can be assigned to E_g modes [64]. The five strong vibrational peaks correspond to the typical frequencies observed for $\alpha\text{-Fe}_2\text{O}_3$ with space group D_{3d}^5 , and the broad features at 1317 cm^{-1} is assigned to two-magnon scattering [65]. However, it is noted that when Fe_2O_3 is exposed to ozone/water vapor flow for 60 min, a new peak at 660 cm^{-1} appears, which originates from the disorder-induced activation of the IR-active mode present at the same wavenumber according to the literature [66,67]. In addition, a new peak occurs at 816 cm^{-1} , which can be assigned to the OO stretching mode of peroxide species (O_2^{2-}) [68–70]. More importantly, the two additional signals enhance with the reaction time extending in ozone/water vapor flow and almost disappear when water vapor is removed, as shown in Fig. 8a. Therefore, it is concluded that the structure of Fe_2O_3 becomes partly disordered when water vapor is introduced in reaction flow, and the catalyst becomes inactive for ozone decomposition. Thereby, the ozone removal rate is hindered and intermediate oxygen species (O_2^{2-}) is accumulated on the surface. When water vapor is cut off, the structure gradually restores and catalytic reaction rate also partly recovers.

On the other side, in-situ Raman spectra of LaFeO_3 presented in Fig. 8b show only the major features of LaFeO_3 perovskite whether in dry air or in RH 90%. The peaks observed below 200 cm^{-1} are related to vibration of La cations. The band observed around 270 cm^{-1} involving two components at 263 and 292 cm^{-1} is assigned to the FeO_6 octahedra tilt (T) modes. The scattering in the 434 cm^{-1} is related to the oxygen octahedral bending vibrations (B). Eventually, the mode observed at 648 cm^{-1} reflects oxygen stretching vibrations (S) together with broader overlapping contributions from longitudinal optic (LO) phonon modes, which is usually reported at 650 cm^{-1} . The broad feature around 1320 cm^{-1} is assigned to second-order scattering [71,72]. Similarly, no new peak besides those of perovskite structure is observed in the in-situ Raman spectra of $\text{LaFe}_{0.95}\text{Ni}_{0.05}\text{O}_3$. The two

additional peaks at 486 and 574 cm^{-1} in Fig. 8c originate from the structural change caused by doping but not by the reaction. To verify this, normal Raman spectra of $\text{LaFe}_{0.95}\text{Ni}_{0.05}\text{O}_3$ and LaFeO_3 are measured without reaction gas flow as shown in Fig. 8d, showing the same peaks as those of Fig. 8c. Therefore, the in-situ Raman spectra of LaFeO_3 and $\text{LaFe}_{0.95}\text{Ni}_{0.05}\text{O}_3$ remain unchanged during different reaction gas flow, suggesting that these LaFeO_3 perovskite structures are stable even in the presence of water vapor and could maintain high ozone removal rate in high RH condition as shown in Figs. 2 and 4.

To further shed light on the crystal difference of Fe_2O_3 and LaFeO_3 catalysts, the crystallography structures are constructed as shown in Fig. 9. $\alpha\text{-Fe}_2\text{O}_3$ is constructed by a hexagonal close-packed oxygen sublattice and only two-thirds of the octahedral interstices are filled with Fe ions [73]. The cationic arrangement generates pairs of FeO_6 octahedra, in which the edges are shared by neighboring octahedra in the same plane and one face in Fe_2O_9 dimers along the c-axis (Fig. 9a) [74,75]. On the other side, LaFeO_3 perovskite is composed of corner-sharing FeO_6 octahedra with the La cations occupying the interstitial area between the octahedral structures (Fig. 9b), playing the stabilizing role in perovskite structure by controlling and modulating the valence and dispersion state of Fe ions [76]. According to Bowley's third law, coordinated polyhedra tend not to share edges, especially not to share faces due to the electrostatic repulsion between the positive ions in the center of two coordination polyhedra. So it could be speculated that LaFeO_3 perovskite structure with corner-sharing FeO_6 octahedra would be more stable than $\alpha\text{-Fe}_2\text{O}_3$, in which the edges are shared by neighboring octahedra [74,75]. As for doped perovskite structure, the incorporation of B-site dopants is necessary for the stability of the material. It is reported that Ni could be the most favorable B-site dopants, due to the low binding energy, suitable thermal expansion coefficient along with the minimal distortion. However, though Mn has typically been assumed to dope on the B-site, it is also found to have significant probability to occupy A-site [77]. This is further verified by the Raman spectra in Fig. 8d, where there are noticeable differences in the

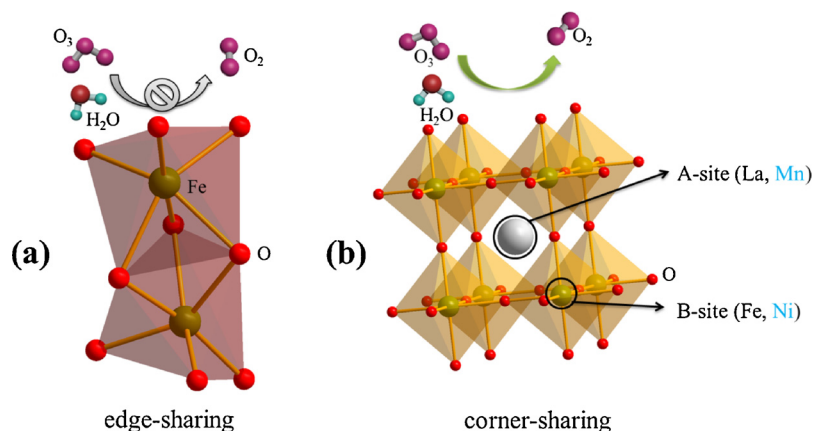


Fig. 9. Structure representations and ozone decomposition illustration of (a) α - Fe_2O_3 and (b) LaFeO_3 .

spectrum of $\text{LaFe}_{0.95}\text{Mn}_{0.05}\text{O}_3$ compared with that of LaFeO_3 and $\text{LaFe}_{0.95}\text{Ni}_{0.05}\text{O}_3$. Firstly, there is a loss of the low frequency A-site vibrations below 200 cm^{-1} , which can be attributed to the A-site disorder and the concurrent lattice distortion induced by the ionic size mismatch. This large lattice distortion is also noticed by the larger 2θ shift of $\text{LaFe}_{0.95}\text{Mn}_{0.05}\text{O}_3$ than that of $\text{LaFe}_{0.95}\text{Ni}_{0.05}\text{O}_3$ in Fig. 3b, though the radius of dopant Mn^{3+} (0.066 nm) is more close to that of Fe^{3+} (0.064 nm) as compared with Ni^{2+} (0.069 nm). Second, there are obvious upshift of 420 cm^{-1} mode and significant resonant enhancement of the 630 cm^{-1} mode in Raman spectrum of $\text{LaFe}_{0.95}\text{Mn}_{0.05}\text{O}_3$, which are typical feature of A-site substitution [78]. Then the low stability caused by competitive occupation of A- and B-sites of Mn ions in $\text{LaFe}_{0.95}\text{Mn}_{0.05}\text{O}_3$ may be responsible for its poor activity on ozone decomposition at high RH in Fig. 4b.

In summary, LaFeO_3 and $\text{LaFe}_{0.95}\text{Ni}_{0.05}\text{O}_3$ present high ozone removal capability and distinct humidity resistance compared with the commonly used Fe_2O_3 analogue. Specifically for $\text{LaFe}_{0.95}\text{Ni}_{0.05}\text{O}_3$, XRD and Raman analyses have shown that Ni is well incorporated into the LaFeO_3 perovskite structure. The intrinsic properties are improved with the introduction of Ni, which then improves the reducibility, redox properties and facilitates desorption of ozone decomposition intermediate, thus enhancing ozone decomposition capability. Furthermore, there are rich adsorption/reaction sites for ozone molecules over $\text{LaFe}_{0.95}\text{Ni}_{0.05}\text{O}_3$ evidenced by NH_3 -TPD. More importantly, H_2O -TPD and in-situ Raman spectroscopy demonstrate that H_2O molecules can be more easily to be desorbed from $\text{LaFe}_{0.95}\text{Ni}_{0.05}\text{O}_3$, and the structure of $\text{LaFe}_{0.95}\text{Ni}_{0.05}\text{O}_3$ remains unchanged during ozone decomposition in the presence of water vapor due to its essential high stability of perovskite structure. As a result, $\text{LaFe}_{0.95}\text{Ni}_{0.05}\text{O}_3$ shows an excellent conversion efficiency of 93% under harsh environment, i.e. RH 90%, 1000 ppm O_3 and at room temperature.

4. Conclusion

A series of mixed oxides LaFe-based perovskite structures are synthesized by citric sol-gel method and tested for ozone catalytic decomposition. Among them, LaFeO_3 and $\text{LaFe}_{0.95}\text{Ni}_{0.05}\text{O}_3$ present high ozone removal capability and distinct humidity resistance compared with the commonly used Fe_2O_3 analogue. Specifically, $\text{LaFe}_{0.95}\text{Ni}_{0.05}\text{O}_3$ shows a high conversion efficiency of 93% under RH 90% and ozone concentration of 1000 ppm at room temperature, while Fe_2O_3 becomes invalid when water vapor is introduced in the reaction. The XPS and in-situ Raman analyses suggest that the structure of Fe_2O_3 turns into disordered under high RH and scarcely reacts with ozone molecular. In contrast, the perovskite structures of LaFeO_3 and $\text{LaFe}_{0.95}\text{Ni}_{0.05}\text{O}_3$ remain stable during ozone decomposition process. Therefore, these LaFe-based perovskite catalysts could still present high ozone removal performance in high RH and high O_3 concentration conditions, which

present great potential for practical applications.

Acknowledgments

This research was financially supported by the National Key R&D Program of China (2016YFC0207100), the Strategic Priority Research Program of the Chinese Academy of Sciences (XDB05050400), the National Natural Science Foundation of China (51672273) and the State Key Laboratory of Multiphase Complex Systems (MPCS-2015-A-04).

Appendix A. Supplementary data

Supplementary material related to this article can be found, in the online version, at doi:<https://doi.org/10.1016/j.apcatb.2018.09.041>.

References

- [1] J.A. Bernstein, N. Alexis, H. Bacchus, I.L. Bernstein, P. Fritz, E. Horner, N. Li, S. Mason, A. Nel, J. Oullette, K. Reijula, T. Reponen, J. Seltzer, A. Smith, S.M. Tarlo, *J. Allergy Clin. Immunol.* 121 (2008) 585–591.
- [2] J.A. Bernstein, N. Alexis, C. Barnes, I.L. Bernstein, J.A. Bernstein, A. Nel, D. Peden, D. Diaz-Sanchez, S.M. Tarlo, P.B. Williams, *J. Allergy Clin. Immunol.* 114 (2004) 1116–1123.
- [3] R. Atkinson, *Atmos. Environ.* 34 (2000) 2063–2101.
- [4] R.S. Keith, *Atmos. Ocean.* 46 (2008) 185–202.
- [5] V. Camel, A. Bermond, *Wat. Res.* 32 (1998) 3208–3222.
- [6] B. Zeynep, K.G. Annel, A.C. Seydim, *Lwt-Food Sci. Technol.* 37 (2004) 453–460.
- [7] B. Saake, R. Lehnen, E. Schmekal, A. Neubauer, H.H. Nimz, *Holzforchung* 52 (1998) 643–650.
- [8] C.J. Weschler, *Environ. Sci. Technol.* 26 (1992) 2371–2377.
- [9] J.W. Charles, *Indoor Air* 10 (2000) 269–288.
- [10] S.T. Oyama, *Catal. Rev.* 42 (2000) 279–322.
- [11] W.T. Tsai, C.Y. Chang, F.H. Jung, C.Y. Chiu, W.H. Huang, Y.H. Yu, H.T. Liou, Y. Ku, J.N. Chen, C.F. Mao, *J. Environ. Sci. Health Part A* 33 (1998) 1705–1717.
- [12] Z.P. Hao, D.Y. Cheng, Y. Guo, Y.H. Liang, *Appl. Catal. B* 33 (2001) 217–222.
- [13] I. Seiichiro, I. Masaaki, *Ind. Eng. Chem. Res.* 30 (1991) 217–221.
- [14] I. Spasova, P. Nikolov, D. Mehandjiev, *Ozone Sci. Eng.* 29 (2007) 41–45.
- [15] W.X. Tang, H.D. Liu, X.F. Wu, Y.F. Chen, *Ozone Sci. Eng.* 36 (2014) 502–512.
- [16] H. Christopher, W.M. Zhang, S.T. Oyama, *Appl. Catal. B* 14 (1997) 117–129.
- [17] Y. Liu, P. Zhang, *Appl. Catal. A* 530 (2017) 102–110.
- [18] J.Z. Ma, C.X. Wang, H. He, *Appl. Catal. B* 201 (2017) 503–510.
- [19] D. Mehandjiev, A. Naidenov, *Ozone Sci. Eng.* 14 (1992) 277–282.
- [20] P.H. Calderbank, J.M.O. Lewis, *Chem. Eng. Sci.* 31 (1976) 1216.
- [21] G. Zhu, J. Zhu, W. Jiang, Z. Zhang, J. Wang, Y. Zhu, Q. Zhang, *Appl. Catal. B* 209 (2017) 729–737.
- [22] J.M. Giraudon, A. Elhachimi, F. Wyrwalski, S. Siffert, A. Aboukais, J.F. Lamonier, G. Leclercq, *Appl. Catal. B* 75 (2007) 157–166.
- [23] R. Mistri, D. Das, J. Llorca, M. Dominguez, T.K. Mandal, P. Mohanty, B.C. Ray, A. Gayen, *RSC Adv.* 6 (2016) 4469–4477.
- [24] S. Royer, H. Alamdari, D. Duprez, S. Kaliaguine, *Appl. Catal. B* 58 (2005) 273–288.
- [25] O.P. Taran, A.B. Ayusheev, O.L. Ogorodnikova, I.P. Prosvirin, L.A. Isupova, V.N. Parmon, *Appl. Catal. B* 180 (2016) 86–93.
- [26] M. Wang, T. Zhao, X. Dong, M. Li, H. Wang, *Appl. Catal. B* 224 (2018) 214–221.
- [27] M. Humayun, N. Sun, F. Raziq, X. Zhang, R. Yan, Z. Li, Y. Qu, L. Jing, *Appl. Catal. B* 231 (2018) 23–33.
- [28] W. Yang, R. Zhang, B. Chen, N. Bion, D. Duprez, S. Royer, *J. Catal.* 295 (2012)

- 45–58.
- [29] K.M. Parida, K.H. Reddy, S. Martha, D.P. Das, N. Biswal, *Int. J. Hydrogen Energy* 35 (2010) 12161–12168.
- [30] R. Spinicci, A. Tofanari, A. Delmastro, D. Mazza, S. Ronchetti, *Mater. Chem. Phys.* 76 (2002) 20–25.
- [31] P. Li, R. Zhang, N. Liu, S. Royer, *Appl. Catal. B* 203 (2017) 174–188.
- [32] X. Li, H. Shi, W. Zhu, S. Zuo, X. Lu, S. Luo, Z. Li, C. Yao, Y. Chen, *Appl. Catal. B* (2018).
- [33] A. Schön, J.-P. Dacquin, P. Granger, C. Dujardin, *Appl. Catal. B* 223 (2018) 167–176.
- [34] S.B. Varandili, A. Babaei, A. Ataie, *Rare Metals* (2016).
- [35] L. Zhang, T. Xu, Q. Guo, Z. Ling, R. Zou, Q. Wu, *J. Phys. Chem. Solids* 110 (2017) 136–144.
- [36] J. Jia, P. Zhang, L. Chen, *Appl. Catal. B* 189 (2016) 210–218.
- [37] G. Zhu, J. Zhu, W. Li, W. Yao, R. Zong, Y. Zhu, Q. Zhang, *Environ. Sci. Technol.* (2018).
- [38] Y. Liu, W. Yang, P. Zhang, J. Zhang, *Appl. Surf. Sci.* 442 (2018) 640–649.
- [39] T. Gopi, G. Swetha, S. Chandra Shekar, C. Ramakrishna, B. Saini, R. Krishna, P.V.L. Rao, *Catal. Commun.* 92 (2017) 51–55.
- [40] Z.H. Lian, J.Z. Ma, H. He, *Catal. Commun.* 59 (2015) 156–160.
- [41] Y. Zheng, K. Li, H. Wang, D. Tian, Y. Wang, X. Zhu, Y. Wei, M. Zheng, Y. Luo, *Appl. Catal. B* 202 (2017) 51–63.
- [42] J.M. Giraudon, A. Elhachimi, G. Leclercq, *Appl. Catal. B* 84 (2008) 251–261.
- [43] J. Faye, A. Baylet, M. Trentesaux, S. Royer, F. Dumeignil, D. Duprez, S. Valange, J.-M. Tatibouët, *Appl. Catal. B* 126 (2012) 134–143.
- [44] S. She, J. Yu, W. Tang, Y. Zhu, Y. Chen, J. Sunarso, W. Zhou, Z. Shao, *ACS Appl. Mater. Interfaces* 10 (2018) 11715–11721.
- [45] K. Zhu, T. Wu, M. Li, R. Lu, X. Zhu, W. Yang, *J. Mater. Chem. A* 5 (2017) 19836–19845.
- [46] S.S. Sable, P.P. Ghute, D. Fakhnasova, R.B. Mane, C.V. Rode, F. Medina, S. Contreras, *Appl. Catal. B* 209 (2017) 523–529.
- [47] Z.X. Wei, Y.Q. Xu, H.Y. Liu, C.W. Hu, J. Hazard. Mater. 165 (2009) 1056–1061.
- [48] F. Fang, N. Feng, L. Wang, J. Meng, G. Liu, P. Zhao, P. Gao, J. Ding, H. Wan, G. Guan, *Appl. Catal. B* 236 (2018) 184–194.
- [49] K.M. Bulanin, A.V. Alexeev, D.S. Bystrov, J.C. Lavalley, A.A. Tsyganenko, *J. Phys. Chem.* 98 (1994) 5100–5103.
- [50] K.M. Bulanin, J.C. Lavalley, A.A. Tsyganenko, *J. Phys. Chem.* 99 (1995) 10294–10298.
- [51] M.A. Henderson, S.A. Joyce, J.R. Rustad, *Surf. Sci.* 417 (1998) 66–81.
- [52] A.A. Alshehri, K. Narasimharao, *J. NanoMater* 2017 (2017) 1–14.
- [53] X.M. Cheng, K.Z. Li, Y.G. Wei, X. Zhu, D. Tian, *Can. J. Chem. Eng.* 95 (2017) 1569–1578.
- [54] Q. Zhang, H. Wang, P. Ning, Z. Song, X. Liu, Y. Duan, *Appl. Surf. Sci.* 419 (2017) 733–743.
- [55] W. Yang, R. Zhang, B. Chen, D. Duprez, S. Royer, *Environ. Sci. Technol.* 46 (2012) 11280–11288.
- [56] L. Dong, Y. Fan, W. Ling, C. Yang, B. Huang, *Catalysts* 7 (2017) 181.
- [57] R. Sumathi, K. Johnson, B. Viswanathan, T.K. Varadarajan, *Appl. Catal. A* 172 (1998) 15–22.
- [58] K. Tabata, Y. Hirano, E. Suzuki, *Appl. Catal. A* 170 (1998) 245–254.
- [59] J. Zhang, X. Weng, Z. Wu, Y. Liu, H. Wang, *Appl. Catal. B* 126 (2012) 231–238.
- [60] W.Y. Hernández, D. Lopez-Gonzalez, S. Ntais, C. Zhao, A. Boréave, P. Vernoux, *Appl. Catal. B* 226 (2018) 202–212.
- [61] B. Dhandapani, S.T. Oyama, *Appl. Catal. B* 11 (1997) 129–166.
- [62] W. Li, G.V. Gibbs, S.T. Oyama, *J. Am. Chem. Soc.* 120 (1998) 9041–9046.
- [63] W. Li, S.T. Oyama, *J. Am. Chem. Soc.* 120 (1998) 9047–9052.
- [64] D.L.A. deFaria, S.V. Silva, M.T. deOliveira, *J. Raman Spectrosc.* 28 (1997) 873–878.
- [65] T.P. Martin, R. Merlin, D.R. Huffman, M. Cardona, *Solid State Commun.* 22 (1977) 565–567.
- [66] D. Bersani, P.P. Lottici, A. Montenero, *J. Raman Spectrosc.* 30 (1999) 355–360.
- [67] S. Onari, T. Arai, K. Kudo, *Phys. Rev. B* 16 (1977) 1717–1721.
- [68] R. Radhakrishnan, S.T. Oyama, *J. Catal.* 199 (2001) 282–290.
- [69] M. Che, A.J. Tench, *Adv. Catal.* 32 (1983) 1–148.
- [70] X.L. Jing, Q.C. Chen, C. He, X.Q. Zhu, W.Z. Weng, W.S. Xia, H.L. Wan, *Phys. Chem. Chem. Phys.* 14 (2012) 6898–6904.
- [71] P.V. Coutinho, F. Cunha, P. Barrozo, *Solid State Commun.* 252 (2017) 59–63.
- [72] D. Blanck, A. Schön, A.-S. Mamede, C. Dujardin, J.-P. Dacquin, P. Granger, J.-F. Paul, E. Berrier, *Catal. Today* 283 (2017) 151–157.
- [73] T. Danno, D. Nakatsuka, Y. Kusano, H. Asaoka, M. Nakanishi, T. Fujii, Y. Ikeda, J. Takada, *Cryst. Growth Des.* 13 (2013) 770–774.
- [74] M. Mishra, D.-M. Chun, *Appl. Catal. A* 498 (2015) 126–141.
- [75] X. Wang, X.Y. Chen, X.C. Ma, H.G. Zheng, M.R. Ji, Z. Zhang, *Chem. Phys. Lett.* 384 (2004) 391–393.
- [76] X. Ren, H. Yang, S. Gen, J. Zhou, T. Yang, X. Zhang, Z. Cheng, S. Sun, *Nanoscale* 8 (2016) 752–756.
- [77] F.H. Taylor, J. Buckeridge, C.R.A. Catlow, *Chem. Mater.* 29 (2017) 8147–8157.
- [78] J. Bielecki, P. Svedlindh, D.T. Tibebu, S.Z. Cai, S.G. Eriksson, L. Borjesson, C.S. Knee, *Phys. Rev. B* 86 (2012) 16.